Sustainable Carbon Materials

https://doi.org/10.48130/scm-0026-0014

Original Research

Open Access

Adsorption of methylene blue dye and potato processing wastewater using bimetallic activated hydrochar: batch and fixed bed column experiments

Milad Jalilian[1], Bisma Nawazish[1], Regiane Taborda[1], Quan Sophia He[2*] and Yulin Hu[1*]

Received: 29 January 2026

Revised: 9 February 2026

Accepted: 13 March 2026

Published online: 8 April 2026

Abstract

Fe-Cu bimetallic activated hydrochar (denoted as MAHC) was prepared from sawdust by hydrothermal carbonization (HTC), KOH activation, and hybridization. Initially, the effectiveness of MAHC on methylene blue (MB) removal was investigated. The fixed-bed adsorption column was then employed to study MAHC's performance in treating MB and potato processing wastewater. Results showed that the highest adsorption capacity of MAHC of 1635.28 mg/g was achieved at pH 10, with 50 ppm MB, 5 ppm MAHC, and 44 °C. The Freundlich model had a better fit than the Langmuir and Temkin models. The pseudo-second-order model provided a better fit than the pseudo-first-order model. The intraparticle diffusion model suggests that higher temperatures lower resistance to mass transfer and allow adsorbate molecules to move faster. Pore filling and surface interactions, such as the interaction between Fe and Cu active sites with MB and π-π interactions, were the dominant mechanisms for MB adsorption onto MAHC. In the fixed-bed column experiments, the breakthrough point was achieved at 165 and 360 min for MB and wastewater, respectively. Overall, this study offers new insights into the removal of pollutants using bimetallic activated hydrochar, as demonstrated by experiments conducted in both batch and fixed-bed column systems.

Keywords: Bimetal, Activated hydrochar, Adsorption, Batch experiments, Continuous experiments

Highlights

- Bimetallic activated hydrochar was synthesized to clean wastewater.
- Adsorption experiments were conducted using both batch and fixed-bed column systems.
- The Freundlich model and the pseudo-second-order model fitted well to the experimental data.
- Pore filling and surface interaction were dominant mechanisms.
- Breakthrough occurred at 165 min for the MB solution, and 360 min for the real wastewater using MAHC.

* Correspondence: Quan Sophia He (Quan.He@Dal.Ca); Yulin Hu (yulinhu@upei.ca)

Full list of author information is available at the end of the article.

https://doi.org/10.48130/scm-0026-0014

Graphical abstract

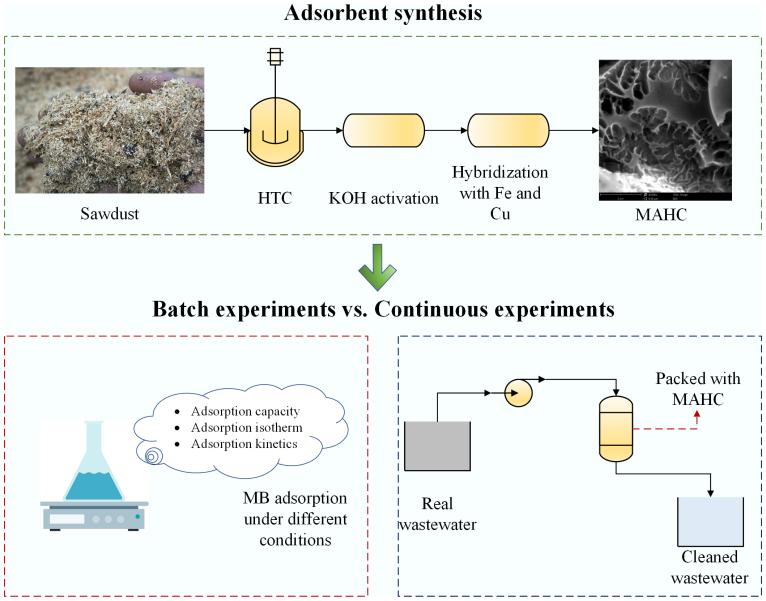

Introduction

For all living organisms to survive, clean water is essential; however, little or no access to clean water exists in certain regions of the world due to increased human activity polluting the water[1]. Therefore, water pollution is one of the significant issues negatively affecting the ecosystem, and posing a major threat to human health. The most common method to treat polluted water is through applying disinfectants, and this has led to more than 100,000 commercially available disinfection products being added to the aquatic environment[2]. The widespread use of disinfectants results in multiple environmental and health concerns. For example, chlorine-containing disinfectants, including sodium hypochlorite, calcium hypochlorite, and chlorine dioxide, can: (1) react with organic contaminants present in water to produce disinfection by-products (DBPs) that exhibit mutagenic, carcinogenic, and teratogenic effects; and (2) promote the mutation of bacterial genes that show strong antibiotic resistance, which pose a great threat to public health upon the spread of such resistance genes among bacteria and accelerate their generation and spreading[3]. As a result, it is important to search for an alternative method to reduce or eliminate the use of disinfectants to clean up wastewater. To date, a variety of wastewater treatment approaches have been established to reduce wastewater discharge and control hazardous pollutants, including physical methods (adsorption, coagulation, and flocculation), biological treatment using enzymes and microbes, and chemical methods (advanced oxidation and ozonation). In recent years, novel approaches like photocatalytic degradation, electro-flocculation, and electro-coagulation have been evaluated[4]. To select the most suitable method, it is essential to consider not only the treatment efficiency but also the energy consumption, cost, and environmental impact.

Among them, carbon-based material adsorption has been regarded as a cost-effective, technologically feasible, easy-to-operate, and non-destructive technique. It has demonstrated excellent performance in adsorbing organic pollutants[5,6], heavy metals[6], antibiotics[7], and pesticides[8]. The most commonly used carbon-based material is activated carbon[9]. Due to increasingly stringent environmental regulations worldwide, the global activated carbon market was valued at US$4.46 billion in 2023 and is projected to reach US$8.41 billion by 2030. The traditional activated carbon production process is composed of: (1) carbonization of organic materials (the most common biomass sources are coconut husks, olive stones, rice husks, and nutshells), typically achieved by pyrolysis under inert conditions to produce carbon-rich precursors, during which the carbon content is increased; and (2) activation of the carbon-rich precursor to create a porous structure by either physical activation (using steam and CO_2) or chemical activation (using KOH and H_3PO_4)[10]. Pore development to create a porous structure in activated carbon plays a critical role in determining its performance, particularly in the adsorption of contaminants in gas and liquid phases. Chemical activation is preferable for producing a widespread, uniform micropore-dominant activated carbon. In contrast, physical activation tends to produce a less uniform micropore structure and a lower yield of activated carbon because the physical activator reacts more readily with carbon particles located on the outer surface rather than in core areas due to diffusion limitations[11]. Therefore, in this work, chemical activation using KOH was chosen. Alternatively, carbon-rich precursors can be produced by hydrothermal carbonization (HTC), which also belongs to thermochemical conversion but is performed at a lower reaction temperature. In addition, HTC offers relatively higher energy efficiency than pyrolysis by avoiding the need for an energy-intensive pre-drying stage given the high moisture content and hygroscopic nature of biomass[12]. HTC is conducted in hot-compressed water at 130–250 °C, and an autogenerated pressure of 1–5 MPa for several minutes to several hours. Owing to the tunable characteristics of water properties, biomass can be converted into well-defined carbon materials with adjustable chemical structures and morphologies[12]. Consequently, HTC, followed by physical/chemical activation to produce activated hydrochar for wastewater treatment, has been explored[13,14]. However, one problem associated with the use of activated hydrochar is its recovery from wastewater, particularly for those with nano-sized particle sizes. One possible solution for tackling this challenge is to introduce magnetic compounds into the carbon structure. In this way, the pore structure and

active sites can be enhanced without affecting the adsorption performance[15]. However, to the best of our knowledge, most studies have focused on the magnetization of biochar or activated biochar, and few studies have explored the influences of the hybridization of bimetallic activated hydrochar on wastewater treatment.

At present, large amounts of organic dyes have been produced and consumed as a result of the increasing global production of textiles, printed materials, and cosmetics[16]. Methylene blue (MB, $C_{16}H_{18}ClN_3S$), which was originally developed in the 1870s, has been extensively applied in a variety of industries, including paper, textiles, cosmetics, and medicine[17]. The presence of MB in aquatic ecosystems prevents light penetration and photosynthesis, thus altering the general equilibrium of aquatic life and disrupting the ecosystems[18]. In addition, MB pollution in drinking water sources causes skin irritation, respiratory problems, and potential cancerous effects from prolonged exposure[19]. Thus, it is important to ensure that MB is removed and that regulatory requirements are met without affecting the ecosystem and human health. Another knowledge gap in the literature is that the majority of studies are only focused on the use of batch experiments and the use of either one or multiple pollutants. However, it is critical to explore the use of a fixed-bed column for the adsorption of contaminants from real wastewater.

To address the above-mentioned problems, this study aims to synthesize Fe-Cu bimetallic activated hydrochar from sawdust using HTC, KOH activation, followed by hybridization. In the first phase of this work, MB adsorption efficiency was evaluated using the synthesized adsorbent at different operating conditions (e.g., pH, temperature, MB concentration, and adsorbent amount) through batch experiments. Next, the effectiveness of this adsorbent in removing contaminants from MB solution and real industrial wastewater was studied in a fixed-bed adsorption column by measuring electrical conductivity and the concentration of total N, P, and K. Finally, a series of analytical instruments were applied to thoroughly characterize the physiochemical properties of bimetallic activated hydrochar.

Materials and methods

Material

The local sawmill in Montague, Prince Edward Island, Canada, supplied the sawdust for this study. Sawdust was pulverized using a grinding machine and sieved to 600 μm. It was then dried in a furnace for 24 h at 100 °C to remove moisture.

All chemicals used in this investigation were acquired from Sigma Aldrich and VWR and used as received.

Hydrochar production

The HTC experiment was carried out in a 1 L HT/HP Parr reactor vessel. Sawdust was mixed with deionized water at a weight ratio of 1:10, and then the slurry was loaded into the reactor. The reactor was properly sealed and flushed with N_2 to eliminate air inside the reactor. The reactor was pre-pressurized using N_2 to ~15 bar. HTC experiments were conducted at 210 °C and kept at this temperature for 4 h. At the end of the reaction, the reactor vessel was cooled to room temperature, and then the gases were removed from the reactor through an exit valve. The reactor was opened, and the solid/liquid mixture was poured into a beaker and filtered under vacuum. Following filtering, the solid hydrocarbon residue on the filter paper was cleaned with deionized water and dried for 24 h at 105 °C.

Activation

The activation procedure and the selected activation parameters were based on our previous work[20]. Briefly, hydrochar was ground with the produced hydrochar at a ratio of 1:2 (hydrochar/KOH) and placed in a lab-built tube furnace (Supplementary Fig. S1). The activation reaction was conducted at 800 °C for 2 h under a continuous N_2 flow at 100 mL/min. After cooling, the produced activated hydrochar was poured into a dilute HCl solution (10 vol.%) and left in the acid for 1 h to remove the unwanted by-products of the reaction. Finally, samples were washed and filtered with deionized water until the pH reached 7, followed by drying in an oven at 105 °C for 24 h.

Hybridization

The synthesis process was carried out as described in our previous study[21]. Briefly, 3 g of activated hydrochar was added to 35 mL of deionized water, followed by adding 1 g of $FeCl_3$ and 0.75 g of $CuSO_4{\cdot}5H_2O$. The mixture was then continuously stirred at 500 rpm for 30 min. In the next step, the solution was heated to 80 °C using a hot plate to create a gel, followed by carbonization in the lab-built tube furnace under an N_2 atmosphere at 300 °C for 2 h. The product was washed using ethanol and deionized water, dried in a furnace at 105 °C for 24 h, ground, and sieved to pass through a 600 μm sieve. The final product was denoted as MAHC.

Batch adsorption experiment

The effects of pH level, adsorbent concentration, temperature, and MB concentration on the adsorption efficiency of MAHC were evaluated. For a typical experiment, MAHC at different concentrations was added to 200 mL of MB solution at different MB concentrations. Dilute KOH and HCl solutions were used to adjust the pH level of the mixture. The mixture was stirred at 500 rpm for 1 h, and the temperature was monitored using a hot plate. Every 10 min, a syringe was used to take a solution, which was then transferred into a cuvette. The absorption was then measured using a UV-Vis spectrometer (V-1200, VWR) at a wavelength of 665 nm, and the concentration of MB was determined using a calibration curve (Supplementary Fig. S2). The adsorption efficiency was calculated using Eq. (1).

$$Adsorption\ efficiency = \frac{C_o - C_t}{C_o} \times 100 \quad (1)$$

where, C_o is the concentration at $t = 0$, and C_t is the concentration at time t.

The adsorption capacity of MAHC was also evaluated at equilibrium time and at any time, q_e (mg/g) and q_t (mg/g), and were determined using Eqs (2) and (3), respectively.

$$q_e = \frac{C_o - C_e}{W} \times V \quad (2)$$

$$q_t = \frac{C_o - C_t}{W} \times V \quad (3)$$

where, C_o is the initial concentration at $t = 0$, C_t is the concentration at time t, C_e is the concentration at equilibrium at time t_e, V (L) is the volume of solution, and W (g) is the mass of MAHC.

Continuous adsorption experiment

To evaluate the effectiveness of the synthesized adsorbent, the real wastewater that was supplied by a local potato processing plant was used as the raw feed in the continuous adsorption experiment. A 50 mL Falcon tube was used as the fixed-bed column for the experiment. This fixed-bed column was packed with 1.5 g of synthesized adsorbent. Before the experiment, the column was equilibrated with a

https://doi.org/10.48130/scm-0026-0014

continuous flow of deionized water using a peristaltic pump (Masterflex L/S, USA). Then, the influent was changed to an MB solution (initial MB concentration of 120 ppm) at a flow rate of 36 mL/min, and effluent sampling was carried out for 180 min. The MB concentration in the effluent was measured using UV-Vis spectrometry (V-1200, VWR) at a wavelength of 665 nm. Following this, the influent was changed to the real wastewater at a flow rate of 6.2 mL/min, and effluent sampling was conducted for 360 min. The total concentrations of N, P, and K, and the electrical conductivity were determined using a handheld tester (CCH0006B-CA, Yitrust, China). The initial concentrations of N, P, K, and the electrical conductivity of this real wastewater are given below in Table 1.

Adsorption isotherms

The experimental equilibrium adsorption data, which are normally presented as isotherms showing the solid phase concentration plotted against the aqueous phase concentration, are correlated using either theoretical or empirical isothermal models. Adsorption isotherms are critical to help understand the interaction between adsorbent and adsorbate and can provide guidance in the optimization of the use of adsorbent. In this study, the Langmuir, Freundlich, and Temkin isotherms were applied to fit the experimental equilibrium isotherm data, and the fitness to each empirical equation was determined using the correlation coefficient R^2.

Langmuir isotherm

Langmuir isotherm is the simplest and most widely used adsorption kinetic model for many sorption processes involving monolayer adsorption, and it assumes that the adsorption sites are energetically homogeneous. Hence, the occupation of one adsorption site does not affect the occupation of another adsorption site[22]. The Langmuir isotherm equations contain constants that represent the adsorbent's affinity and surface characteristics. The Langmuir isotherm equation is given in Eq. (4)[23].

$$\frac{C_e}{q_e} = \frac{1}{q_m} C_e + \frac{1}{k_L . q_m} \tag{4}$$

where, C_e (mg/L) is the concentration of adsorbate (i.e., MB) at equilibrium, and q_e (mg/g) is the adsorption capacity at equilibrium. The maximal adsorption capacity (mg/g) is denoted by q_m. The Langmuir adsorption constant is denoted by k_L. Plotting C_e/q_e against C_e gives a straight line, and the resulting slope and intercept are used to determine q_m and k_a.

Freundlich isotherm

The Freundlich isotherm is an empirical equation that describes a model in which the surface of the adsorbent is heterogeneous with varied adsorption energies, unlike in the Langmuir isotherm. The Freundlich isotherm can only be applied in low to intermediate concentrations of adsorbate since it does not imply a finite uptake capacity of adsorbate[24]. Equation (5) describes the Freundlich isotherm.

$$ln q_e = ln k_f + \frac{1}{n_f} ln C_e \tag{5}$$

Table 1 Analysis of real wastewater provided by a local potato processing facility

Property	Value
Electrical conductivity (µs/cm)	2,961
Total nitrogen (mg/g)	588
Total phosphorus (mg/g)	1,219
Total potassium (mg/g)	1,269

where, k_f is the Freundlich constant (mg/g)(L/mg)$^{1/nf}$) and $1/n_f$ is an empirical parameter that correlates the adsorption intensity with adsorbent heterogeneity. Plotting of lnq_e against lnC_e yields a straight line, and the slope and intercept can be used to determine $1/n_f$ and k_f, respectively.

Temkin isotherm

Even though the Temkin isotherm is not as popular as the Langmuir and Freundlich isotherms, it is often applied to model water contaminant adsorption and is compared with the Langmuir and Freundlich isotherms. The Temkin isotherm considers the effects of the interaction between the adsorbent and adsorbate, and is only valid for an intermediate range of concentrations. It assumes that the heat of adsorption decreases linearly with increasing surface coverage, reflecting that the interaction between the adsorbent and adsorbate becomes more pronounced as more adsorbate molecules accumulate on the surface of the adsorbent, which results in a decrease in the overall heat of adsorption[25]. It is described using Eq. (6).

$$Q_e = \frac{RT}{b_T} \times ln k_t + \left(\frac{RT}{b_T}\right) \times ln C_e \tag{6}$$

where, R is the universal gas constant (J/(mol·K)), T is the temperature (K), b_T is the parameter related to the adsorption energy (J/mol), and k_T is the adsorption equilibrium constant (1/Pa).

Adsorption kinetics

Pseudo-first-order model

The pseudo-first-order model was proposed by Lagergen in 1898[26], and describes the rate of adsorption in accordance with the assumption that the adsorption rate depends on the diffusion of adsorbate on the adsorbent surface, and is proportional to the difference between the amount adsorbed at equilibrium and the amount adsorbed at time t. This model is widely used when the rate-limiting step is diffusion, which is often associated with physisorption[27]. The empirical equation is given as follows:

$$ln (q_e - q_t) = ln q_e - k_1 t \tag{7}$$

where, q_e and q_t are the adsorption capacities at equilibrium and at time t, respectively. k_1 is the pseudo-first-order model equilibrium rate constant.

By plotting $\ln(q_e - q_t)$ vs time t, the slope of the straight line gives k_1.

Pseudo-second-order model

The pseudo-second-order model is normally applied to describe adsorption processes that take a longer time to fill the adsorption sites. The assumption made in the pseudo-second-order model is that the adsorption process, particularly the rate-limiting step, involves chemisorption where the interaction between adsorption sites on the adsorbent surface and adsorbate, involving electron transfer, can be observed[27,28]. The linearized form of this model is given below.

$$\frac{t}{q_t} = \frac{1}{k_2 q_e^2} + \frac{t}{q_e} \tag{8}$$

where, q_e and q_t are the adsorption capacities at equilibrium and at time t, respectively. t is the time. k_2 is the pseudo-second-order model equilibrium rate constant.

Intraparticle diffusion model

The intraparticle diffusion model, also known as the Weber-Morris model, describes the rate-limiting step in the adsorption process where the molecules diffuse into the internal pores of an adsorbent. Equation (9) can be used to illustrate this model:

$$q_t = k_t t^{1/2} + C \tag{9}$$

Characterizations of MAHC

The surface structure of MAHC was initially determined using a Brunauer-Emmett-Teller (BET) analyzer (Microtrac MRB BELSORP-Mini X). The surface morphology and elemental composition were determined by scanning electron microscopy (SEM) coupled with energy-dispersive X-ray spectroscopy (EDX) at Western University (London, Canada). A CHNS analyzer (Flash 2000, Thermo Scientific) was utilized to determine the C, H, O, N, and S content. Thermal degradation characteristics were determined by using a PerkinElmer TGA 4000 to heat from 30 to 800 °C in air at a heating rate of 10 °C/min, and an air flow rate of 30 mL/min, respectively. The iodine number was measured according to ASTM D4607-14[29]. The zeta potential at varying pH levels was measured using a 1 mg/mL sample at 25 °C with a Zetasizer Nano ZS (Malvern Instruments, UK). FTIR spectra of sawdust, hydrochar, activated hydrochar, and hybridized activated hydrochar were recorded using a Spectrum Two FTIR (PerkinElmer, US) over the range of 4,000 to 400 cm^{-1} with a resolution of 4 cm^{-1}.

Results and discussion

Characterization results of MAHC

The adsorption and desorption curves of MAHC and its pore size distribution are given in Fig. 1. As shown in Fig. 1a, it can be found that the quantity of adsorbed adsorbate (i.e., N_2) increases sharply at the low pressure range and then plateaus, reaching a saturation limit, which suggests that this adsorption isotherm belongs to Type I and MAHC is a microporous solid. This observation was also reported in the study of activated hydrochar derived from coffee husk waste for MB removal[30]. The BET surface area and total pore volume of MAHC were determined to be 1,266.1 m^2/g and 0.7394 cm^3/g, respectively. In comparison, it is observed that the specific surface area of activated carbon derived from peach stone is 915 m^2/g, and the total pore volume is 0.477 cm^3/g[31]. This is mainly due to the differences in the activation method, where physical activation using steam was applied. Based on the Non-Local Density Functional Theory (NLDFT) and Grand Canonical Monte Carlo (GCMC), the pore size distribution of MAHC was obtained, and it can be clearly seen that the dominant pore size range is within 0–2 nm, which belongs to the micropore range.

SEM is used as an important tool to understand the surface morphology, the porosity development, and surface structure of MAHC. The obtained SEM images are given in Fig. 2. The SEM images show that MAHC has an irregular, rough, and porous surface, which is commonly observed on the surface of activated carbon[32]. This porous structure with numerous cavities and pores plays a significant role in the adsorption of MB as an adsorbent. The right-hand SEM image at a magnification of 19,000× shows bright spots on the surface of MAHC, which could be related to the introduced Fe and Cu nanoparticles. To confirm this, EDX analysis was also carried out for MAHC. As indicated in Fig. 3, the EDX spectrum of MAHC exhibits the presence of C and O, along with peaks for Fe and Cu. The detection of Fe and Cu suggests the successful incorporation of Fe and Cu nanoparticles during the synthesis process. It can also be found that no K can be observed in the EDX spectrum where KOH was added as a chemical activator. This could imply that acid washing in the synthesis step was complete, and then a cleaner carbon material was produced, thereby resulting in a very low, or even undetectable, K signal in the EDX spectrum.

To investigate the surface chemistry, the FTIR spectra of sawdust, hydrochar, activated carbon, and hybridized activated carbon are shown in Fig. 4. It can be found that the sawdust and hydrochar showed significant differences in surface functionality; however, no significant differences can be observed in the functional groups on the surface of activated carbon and MAHC. Another major observation is that the functional groups on activated carbon and MAHC are fewer than those of sawdust and hydrochar, which could be due to the high-thermal treatment during the activation step (i.e., 800 °C for 2 h). As indicated in Fig. 4c, d, the peak at 3,667 cm^{-1} could be related to the –OH group, and peaks at 3,000–2,840 cm^{-1} could be attributed to the C–H stretching vibration in alkanes. Besides, the peaks between 1,085 and 1,050 cm^{-1} can be observed in both samples, which could be due to the presence of the C–O stretching vibration present in alcohols. When compared to other activated carbons, and Cu-, Fe-, or Fe/Cu-doped carbon materials, it can be observed that a higher number of functional groups are present. For instance, rice straw-derived activated carbon showed clear peaks corresponding to C=O (1,630 cm^{-1}) and C–C (1,370 cm^{-1}), which were absent in our hybridized activated carbon[33]. This could be due to the differences in the activation methods, where this study applied wet impregnation methods and extremely mild reaction conditions (0.1 M H_2SO_4 treatment at room temperature, followed by 0.2 M KOH at 25 °C for 24 h). In another study, Cu co-doped

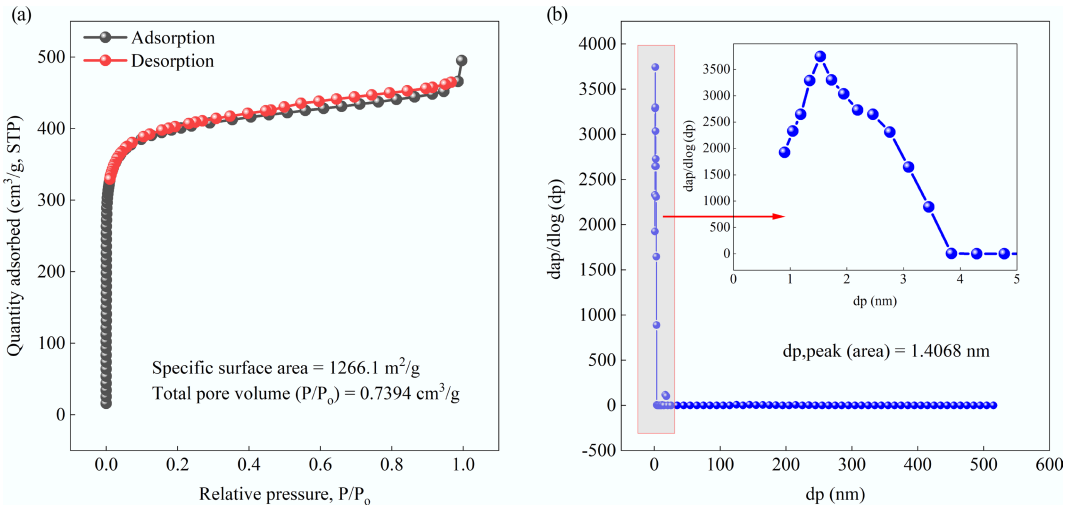

Fig. 1 (**a**) Adsorption and desorption curves, and (**b**) pore size distribution of MAHC.

https://doi.org/10.48130/scm-0026-0014

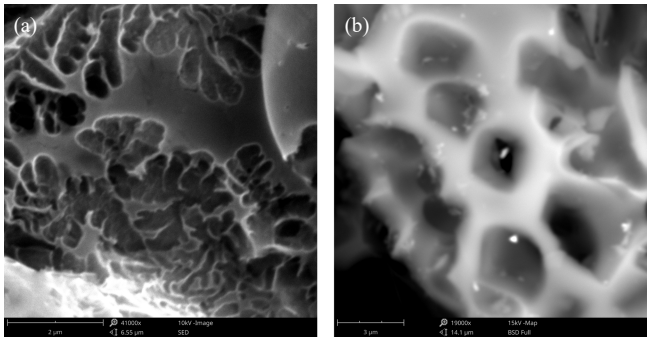

Fig. 2 SEM images of MAHC at different magnifications. (**a**) 41,000×, and (**b**) 19,000×.

activated carbon was prepared for MB removal, and FTIR analysis results indicated that two peaks at 1,750 and 1,500 cm^{-1}, which could represent C=O from carbonyl groups, were observed[34]. Similar to the reason mentioned earlier, aside from the difference in the synthesis method, the low concentration of such functional groups in MAHC makes their detection unachievable by FTIR analysis.

The thermal degradation characteristics of hybridized activated carbon (i.e., MAHC) in air are shown in Fig. 5. The thermal degradation profile indicates that MAHC showed a slight weight loss of 2.15% at temperatures below 110 °C, which could be mainly related to moisture removal. Two major weight loss stages were observed, peaking at 336 and 386 °C, respectively. This could be owing to the oxidation of carbon. After oxidation, a residual mass of ~7.16 wt.% of the original weight was observed, which could be related to iron oxide and copper oxide[35].

CHNS results of sawdust, hydrochar, activated carbon, and hybridized activated carbon are summarized in Table 2. Based on the elemental composition results, the Van Krevelen diagram is displayed in Fig. 6. It can be seen that the C content of MAHC was ~79 wt.%, which is higher than that reported in a previous study where the C content of Fe-doped activated carbon from almond shells was 50.48 wt.%–58.78 wt.%. Compared with commercial activated carbon-based adsorbent for wastewater treatment, it can be found that the C content of both MAHC and activated hydrochar is

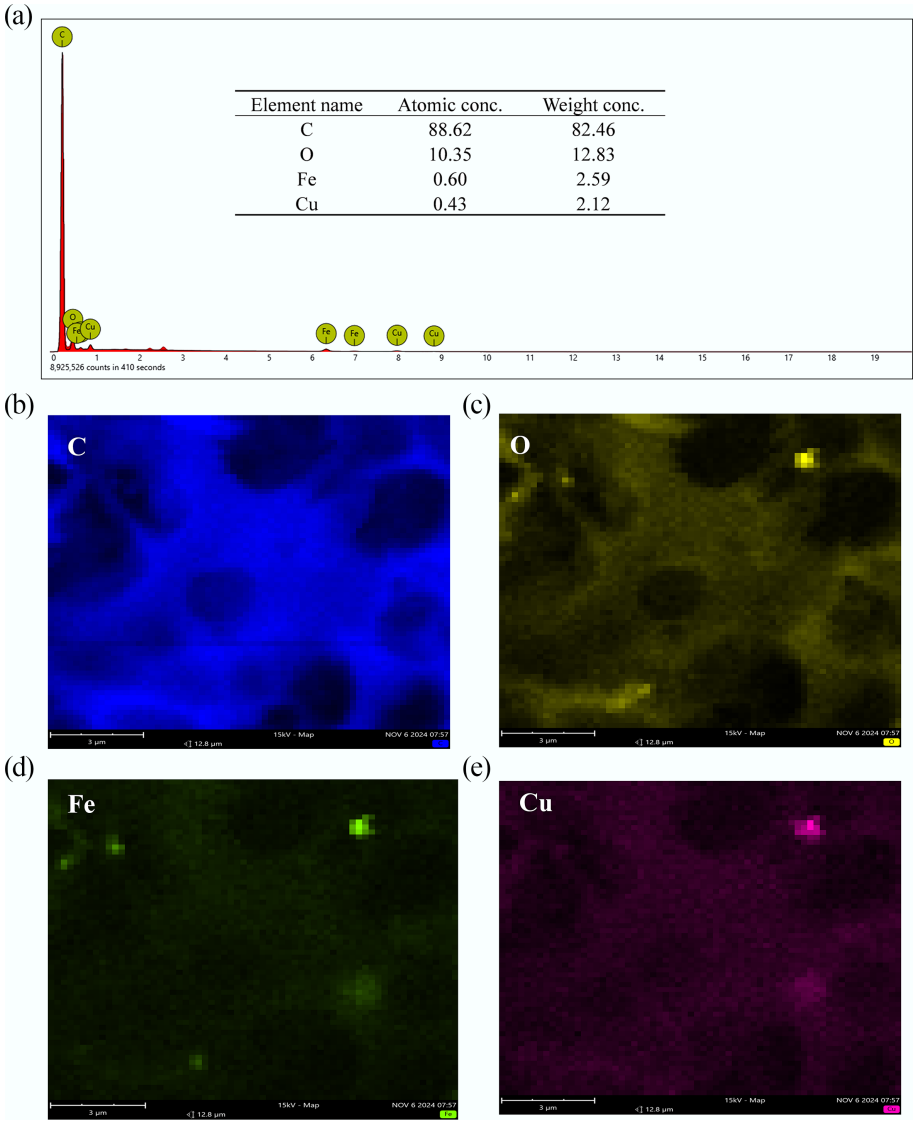

Fig. 3 (**a**) EDX results of MAHC element composition at the surface, (**b**) C, (**c**) O, (**d**) Fe, and (**e**) Cu.

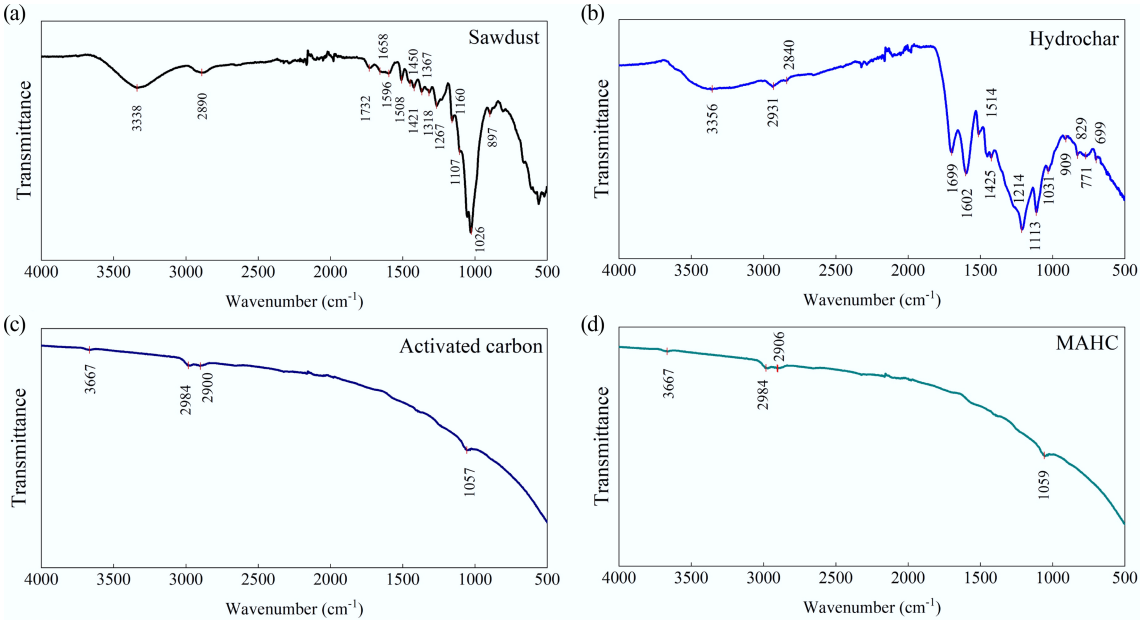

Fig. 4 FTIR spectra of (**a**) sawdust, (**b**) hydrochar, (**c**) activated carbon, and (**d**) and MAHC.

comparable. A high C content may suggest a higher adsorption performance due to better mechanical strength, lower impurity levels, and better chemical inertness, and could contribute to a more developed internal pore structure and hence more adsorption sites for pollutant adsorption. An ash content of 7.16 wt.% was observed in the MAHC, which could be related to the integration of Fe and Cu into the C matrix. Interestingly, it can be found that activated hydrochar contained 10.70 wt.% of ash, which could be caused by the presence of ash in sawdust, and the unwashed K-containing impurities during the KOH activation process. In the KOH activation process, the following chemical reactions could occur.

$$4KOH + C \leftrightarrow 4K + CO_2 + 2H_2O \quad (10)$$

$$4KOH + 2CO_2 \leftrightarrow 2K_2CO_3 + 2H_2O \quad (11)$$

Iodine number is an indicator for the adsorption performance of activated carbon and is well accepted as a rapid assessment method to determine its quality. The porosity can be characterized by iodine number analysis, and the iodine number result of MAHC was determined to be 612.3 mg/g, as given in Table 3. In general, the iodine number of standard activated carbon falls within the range of 500–1,200 mg/g, and a higher adsorption rate usually can be found in an activated carbon with a higher iodine number. The iodine number of MAHC can be observed to fall within the range of standard activated carbon and is comparable to the results of commercial activated carbon. Compared with the literature, it can be seen that the MAHC provided a higher iodine number than activated carbon derived from sludge with different chemical activating agents. This could be due to the differences in the surface area and micropore volume.

Zeta potential is the potential difference between the dispersion medium and the stationary layer of fluid attached to the dispersed particle. It can provide information regarding the surface charge, and the stability of particles, as well as the interaction between solid particles and the bulk phase of the liquid. The results are provided in Fig. 7. The zeta potential of MAHC in the tested pH range (pH = 3–11) was between +11.16 and −55.61 mV. Generally, activated carbon, like MAHC, is considered an amphoteric solid that can react with both acids and bases depending on the surrounding environment, which is owing to the presence of various functional groups on the solid surface. The isoelectric point (pI) , which can be used to qualitatively determine the polarity of the surface charge of the adsorbent, is defined as the pH at which a molecule has no net

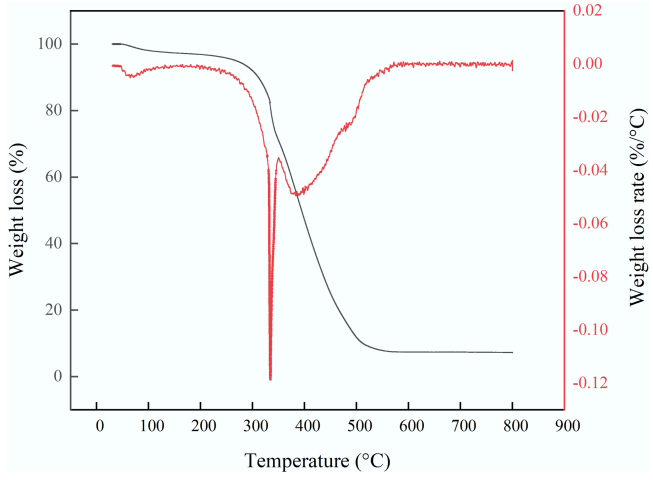

Fig. 5 Thermal degradation characteristics of MAHC.

Table 2 Elemental composition of sawdust, hydrochar, activated hydrochar, and MAHC

	C	H	O[1]	N	S[2]	Ash[3]
Sawdust	47.76	5.90	44.34	n.d.	n.d.	2.00
Hydrochar	53.45	3.28	38.18	n.d.	n.d.	5.09
Activated hydrochar	78.42	2.72	7.88	0.28	n.d.	10.70
MAHC	79.13	1.26	12.23	0.22	n.d.	7.16

[1] Oxygen content was estimated by difference. [2] n.d. represents not detectable. [3] Ash content was measured using thermal gravimetric analysis in air up to 900 °C and held at 900 °C for 30 min.

https://doi.org/10.48130/scm-0026-0014

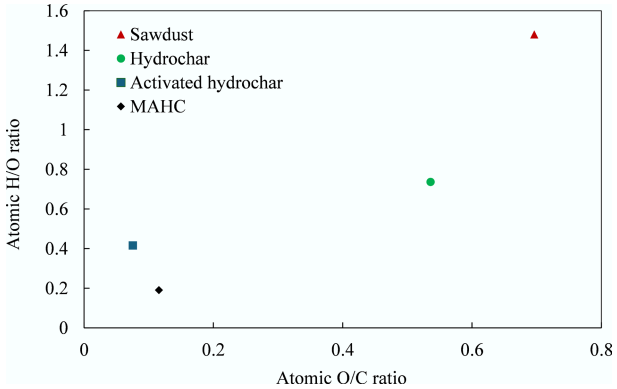

Fig. 6 Van Krevelen diagram.

electrical charge. pI can be determined as the pH value at which the zeta potential becomes zero. Figure 7 shows that the pI of MAHC is ~5.1. At pH < pI, the surface charge of the adsorbent is positive, and thus is favorable for adsorbing anions, while at pH > pI, the surface charge of the adsorbent is negative and hence is beneficial for adsorbing cations[38]. In terms of stability of nanoparticles, a zeta potential with an absolute value greater than 30 mV is critical to ensure their stability in a suspension, as it implies that the electrostatic repulsion between nanoparticles is sufficiently strong to prevent aggregation[39]. The results show that the absolute value of the zeta potential of MAHC is above 30 mV at pH values > ~9.5, suggesting that the Fe-Cu nanoparticles in the activated carbon matrix are colloidally stable.

Effect of operational parameters on MB adsorption

Preliminary test

In a preliminary experiment, the effect of pH on the adsorption performance of MAHC was investigated at three different pH levels of 4, 7, and 10 at 24 °C. Briefly, MAHC samples in three different concentrations (25, 50, and 75 ppm) were added to a 200 mL aliquot of preprepared 5 ppm MB solution. The resultant adsorption efficiency is given in Fig. 8. It can be observed that at a fixed concentration of MAHC, the effect of pH level on adsorption efficiency was minor. This result could suggest that the surface charge (either positively or

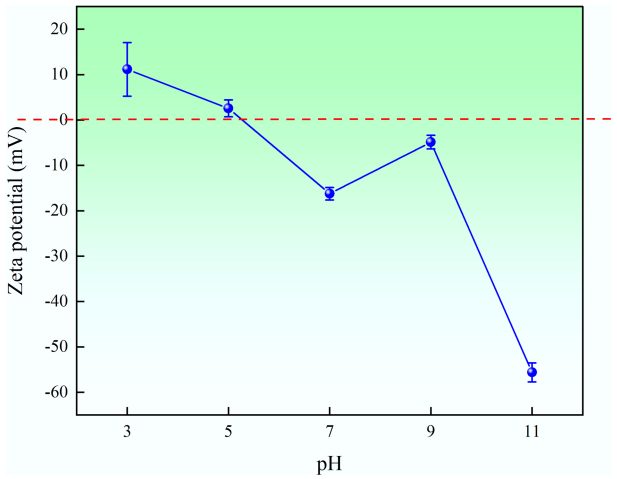

Fig. 7 Zeta potential results of MAHC at different pH levels.

Table 3 Iodine number of MAHC compared with the literature and commercial activated carbon

Iodine number	Value (mg/g)
This study	612.3
Sludge-derived activated carbon using $ZnCl_2$[36]	531.8
Sludge-derived activated carbon using KCl[36]	376.0
Sludge-derived activated carbon using $ZnCl_2$ and H_2SO_4[36]	446.9
Sludge-derived activated carbon using $ZnCl_2$ and KOH[36]	363.9
Sludge-derived activated carbon using KOH[36]	439.0
Acorn shell-derived activated carbon using $ZnCl_2$[37]	37–1,209
Calgon carbon (powdered activated carbon)	> 500
CS corporation (powdered activated carbon)	500–2,500

negatively charged) does not significantly affect the MB adsorption, and thus, electrostatic attraction is actually not the governing mechanism in the adsorption of MB onto MAHC. On the other hand, with an increase in MAHC concentration, the adsorption efficiency of MB increased proportionally. Similar results were reported by Altıntıg et al.[40]. The increase in adsorbent amounts leads to an increase in the number of available adsorption sites and surface area, thereby enhancing MB adsorption efficiency. This could also explain why adsorption efficiency almost reached 100% at 75 ppm MAHC across all studied pH levels. Overall, together with the zeta potential results, the pH level of 10 was selected for the following batch adsorption experiment.

Batch adsorption experiments

Next, batch adsorption experiments were redesigned after selecting the pH based on the preliminary results. Initially, batch adsorption was carried out at two different concentrations (10 and 50 ppm) of MB, and the adsorption capacity of 10 mg of MHAC in 1 L of MB solutions (or 10 ppm) was investigated at pH 10 and 24 °C. The results are given in Fig. 9a. Although there was no significant difference between the MB adsorption capacity for different concentrations at t < 12 h, the increase in the MB concentration enhanced the adsorption capacity at t = 23 h. This trend was also previously reported by Karaer & Kaya[41]. At t = 23 h, the adsorption capacity obtained at 10 ppm MB and 50 ppm MB was 410.6 and 481.6 mg/g, respectively. This result is attributed to the higher concentration gradient of MB between the solution and the adsorbent surface, which increases the driving force for mass transfer at higher MB concentrations and promotes the interaction between MB and the adsorbent's surface, thereby resulting in a higher MB adsorption capacity[42]. One interesting finding is that the adsorption by MAHC slowly reached a plateau after 23 h, but continued to increase in adsorption capacity for MB at 50 ppm after 23 h. Compared to the literature, either hybridized activated carbon or activated composite can reach a plateau in terms of adsorption capacity within 1 or 2 h[41,42]. This could indicate that the adsorption rate of our adsorbent is much lower than that of other materials reported in the literature, and thus it is not kinetically optimal. One possible reason could be related to the highly microporous structure of MAHC, as indicated in the pore size distribution plot (Fig. 1b), since the smaller pore size restricts the movement of adsorbate molecules and thus, slows down their diffusion to the internal surface area for adsorption, like the MB molecule (1.7 nm × 0.76 nm × 0.33 nm). This leads to slow adsorption kinetics, and overall mass transfer will be limited for larger adsorbates. This can be proven by the average pore diameter of activated carbon and magnetic activated carbon of 3.78–4.16 nm reported in the literature, in which the adsorption capacity reached a plateau within 100 min[42]. The concentration of MB of 50 ppm was chosen for the following investigation on the influence of the adsorbent amount on the adsorption capacity.

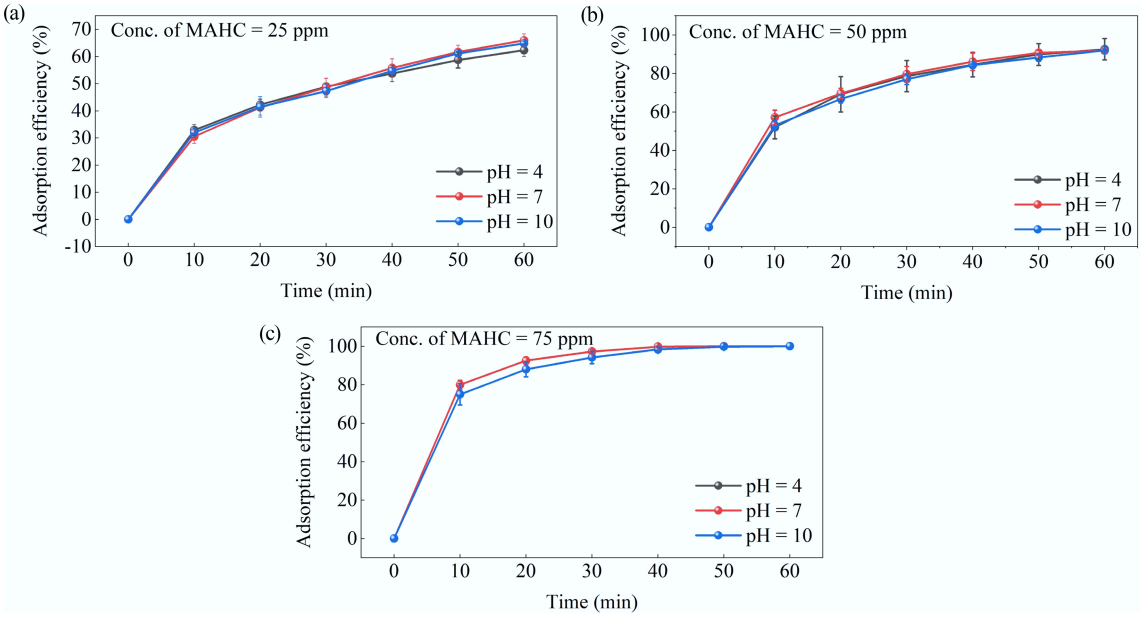

Fig. 8 Effect of pH level on the adsorption efficiency of MAHC obtained at MB concentration of 5 ppm, 24 °C, and (**a**) 25 ppm MAHC, (**b**) 50 ppm MAHC, and (**c**) 75 ppm MAHC.

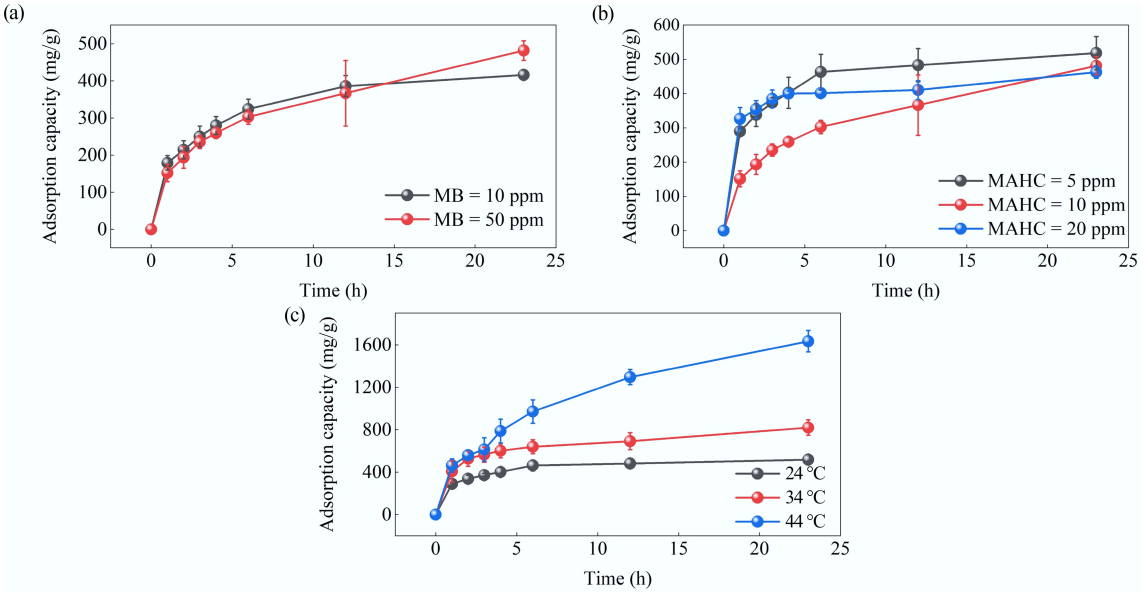

Fig. 9 Effect of (**a**) MB concentration, (**b**) MAHC amount, and (**c**) temperature on adsorption capacity.

The adsorbent concentration is another significant factor that affects MB adsorption capacity, and its effect was explored at 24 °C, pH 10, an MB concentration of 50 ppm, and using three adsorbent amounts: 5, 10, and 20 ppm. The results are shown in Fig. 9b. It can be seen that the adsorption capacity decreases with increasing adsorbent amount, which is in good agreement with the literature[43]. This is because the amount of MB to be adsorbed remains constant at the different MAHC amounts studied, while the total number of available adsorption sites increases with increasing MAHC amounts, thereby resulting in a lower amount of MB adsorbed per unit mass of adsorbent.

The effect of temperature on the adsorption of MB was studied at a pH of 10, an MB concentration of 50 ppm, an MAHC amount of 5 ppm, and three different temperatures of 24, 34, and 44 °C, and the results are depicted in Fig. 9c. The results showed that the highest adsorption capacity of MAHC of 1,635.28 mg/g was achieved at a pH of 10, with 50 ppm MB solution, 5 ppm MAHC, and 44 °C. It can be found that the adsorption capacity was proportional to temperature, implying the endothermic nature of this adsorption process. This is because the adsorption of MB onto hybridized activated carbon is not just a simple physisorption process, but instead a combination of physisorption and chemisorption. The trend was also previously reported by Yao et al.[44] and Ghaedi et al.[45]. Additionally, it should be noted that a big increase in adsorption capacity can be observed when increasing the temperature from 24 to 44 °C. This implies that a higher temperature is required to enhance the adsorption performance of MAHC; however, this leads to a potential limitation of the use of MAHC in wastewater and possibly

https://doi.org/10.48130/scm-0026-0014

water purification. In industrial practice for wastewater treatment or water purification, the adsorption of contaminants is typically conducted at or near room temperature. In future studies, it is important to modify the MAHC material to improve its kinetics and adsorption capacity at or near room temperature.

Compared with other adsorbents for removing MB from solution, our adsorbent materials showed comparable or superior adsorption capacity. Hien Tran et al.[46] reported that the maximum MB adsorption capacity was 489.56 mg/g for KOH-activated hydrochar derived from corncob. In another study, at 30 °C, Qian et al.[47] observed that the highest MB adsorption capacity of 655.76 mg/g was achieved using NaOH- and chlorane-modified hydrochar. In a study by Islam et al.[48], it was found that the highest adsorption capacity for MB was 200.01 mg/g at 30 °C when using NaOH-activated coconut shell-derived hydrochar.

Adsorption isotherms

The Langmuir, Freundlich, and Temkin adsorption isotherms for MB adsorption onto MAHC, and the associated computational parameters are presented in Fig. 10a–c and Table 4, respectively. The results indicated that the Freundlich model (R^2 = 0.97576) fits the experimental data better than the Langmuir and Temkin models (R^2 = 0.6629 and 0.97114, respectively). This implies that the Freundlich model is more suitable for describing the adsorption behavior of MB on the MAHC. In contrast to much of the literature, this work demonstrated that the adsorption behavior of MB on the MAHC did not fit well with the Langmuir model, which is widely reported to fit well with adsorption experiments using carbon-based materials[32, 49]. According to this result, it can be stated that multilayer adsorption on a heterogeneous surface with a non-uniform distribution of adsorption heat is more dominant in MB adsorption using MAHC than monolayer adsorption on a homogeneous surface with uniform adsorption sites. The Freundlich adsorption isotherm parameters, including the dimensionless constant k_F and n, represent the capacity and intensity of the adsorption, respectively. As shown in Table 4, the value of n is above 1, indicating that the adsorption of MB onto MAHC is favorable[50]. Al-Musawi & Al-Qaim[51] used waste fig fruits to prepare activated carbon for MB adsorption and found that the adsorption process fitted the Freundlich isotherm better than the Langmuir isotherm. A similar finding was previously reported by Buhani et al.[52], who utilized rubber fruit shells as raw materials to fabricate adsorbent materials.

Adsorption kinetics

The adsorption kinetics of MB onto MAHC were initially evaluated using the pseudo-first-order and pseudo-second-order models at 24–44 °C, pH 10, in a 50 ppm MB solution, and with an MAHC amount of 5 ppm. Both models can help determine whether the interaction between the adsorbate and active sites on the MAHC's surface is chemical or physical in nature, and the resulting model parameters and linear plots are given in Figs 11 and 12, respectively. The associated kinetic model fitting parameters for MB adsorption on MAHC are summarized in Table 5. The pseudo-first-order and pseudo-second-order models showed fitness with experimental data, with correlation coefficient (R^2) values in the range of 0.739–0.980, and 0.978–0.999, respectively. It can be clearly seen that the pseudo-second-order model provided a better fit than the pseudo-first-order model, implying that the chemisorption is a rate-limiting step for the MB adsorption onto MAHC. As shown in Table 5, the calculated q_e values from pseudo-second-order model were also in good agreement with experimental values (see Fig. 9). Similar findings were previously reported by Lyu et al.[53]. The pseudo-second-order model was also identified to be the most suitable kinetic model when using activated carbon derived from *Coriandrum sativum* to adsorb MB[54]. Typically, the pseudo-second-order model is more accurate than the pseudo-first-order model, since the pseudo-first-order model assumes the rate of adsorption is controlled by the number of available active sites, whereas the pseudo-second-order model considers the interaction between the adsorbate and adsorbent.

Next, the intraparticle diffusion model was taken into consideration. The relevant kinetic model fitting parameters are provided in Table 6. In Fig. 13, it can be seen that three linear segments can be clearly observed at 24 and 34 °C, which indicates that MB adsorption onto MAHC involves three stages. In the first step, the adsorbate diffuses quickly through the thick, static fluid film (the

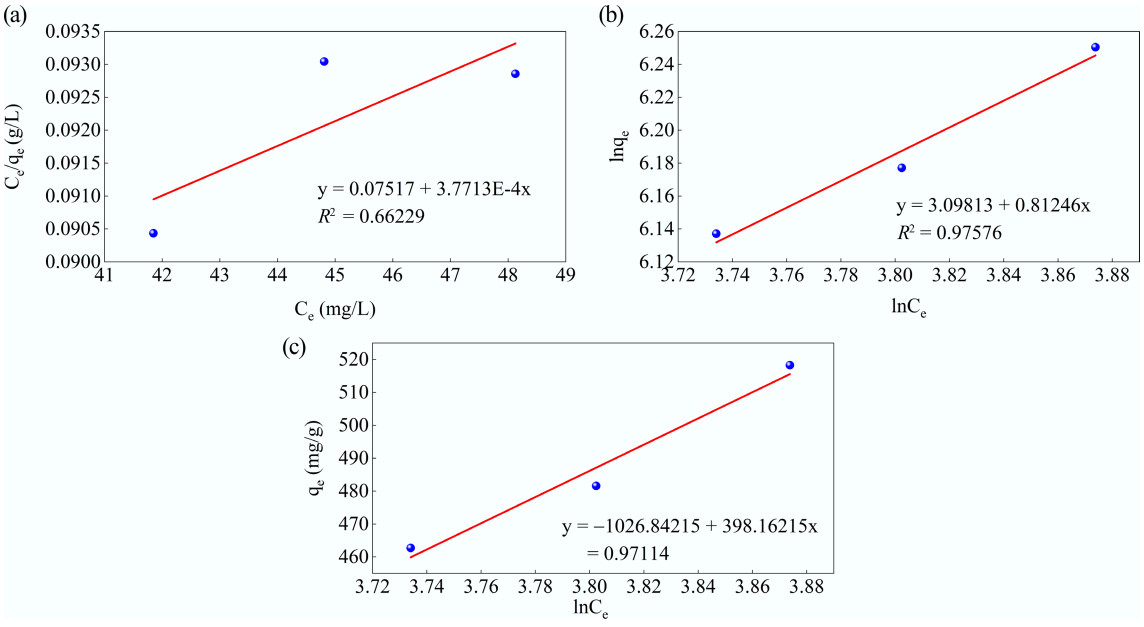

Fig. 10 (a) Langmuir, (b) Freundlich, and (c) Temkin adsorption isotherms for MB adsorption at 50 ppm MB, pH = 10, MAHC = 5–20 ppm, and 24 °C.

Table 4 Isotherm model parameters

Isotherm model	Parameter	Values
Langmuir	q_m (mg/g)	2,651.606
	k_L(L/mg)	0.005017
	R^2	0.66229
Freundlich	$1/n_f$	0.81246
	k_f (mg/g)(L/mg)$^{1/n}$	22.15648
	R^2	0.97576
Temkin	b_t	0.006205
	k_T (L/mg)	0.075853
	R^2	0.97114

boundary layer) to the external adsorbent surface, which is characterized by a higher intraparticle diffusion rate (K_p) than the second and third stages (Table 4). The second stage occurs when the adsorbate molecules diffuse into the internal pores of the MAHC. Finally, the third stage reaches equilibrium, where the low residual adsorbate moves slowly from larger pores to smaller pores (micropores), which is characterized by the lowest value of K_p (Table 4). The constant C is related to the boundary layer thickness. In general, it can be found that the constant C at the second and third stages is larger than that at the first stage, suggesting a thicker boundary layer and a longer diffusion path, which contributes to a greater resistance to mass transfer[32,55]. When the temperature increases to

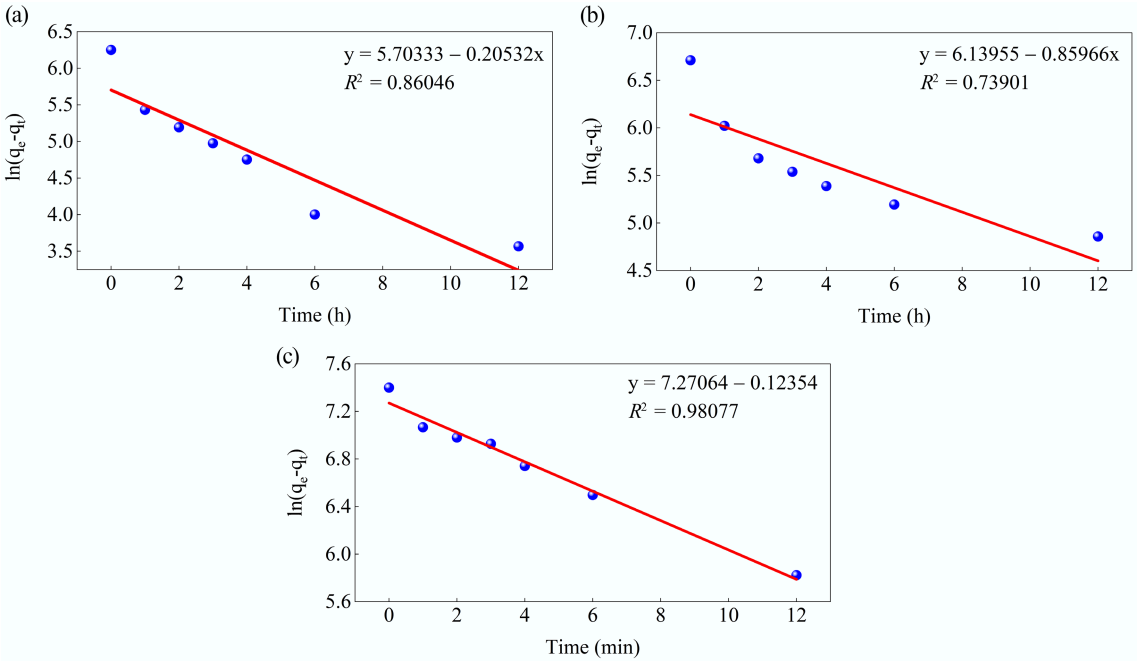

Fig. 11 Kinetic fits for MB adsorption on MAHC at (**a**) 24 °C, (**b**) 34 °C, and (**c**) 44 °C, using the pseudo-first-order model.

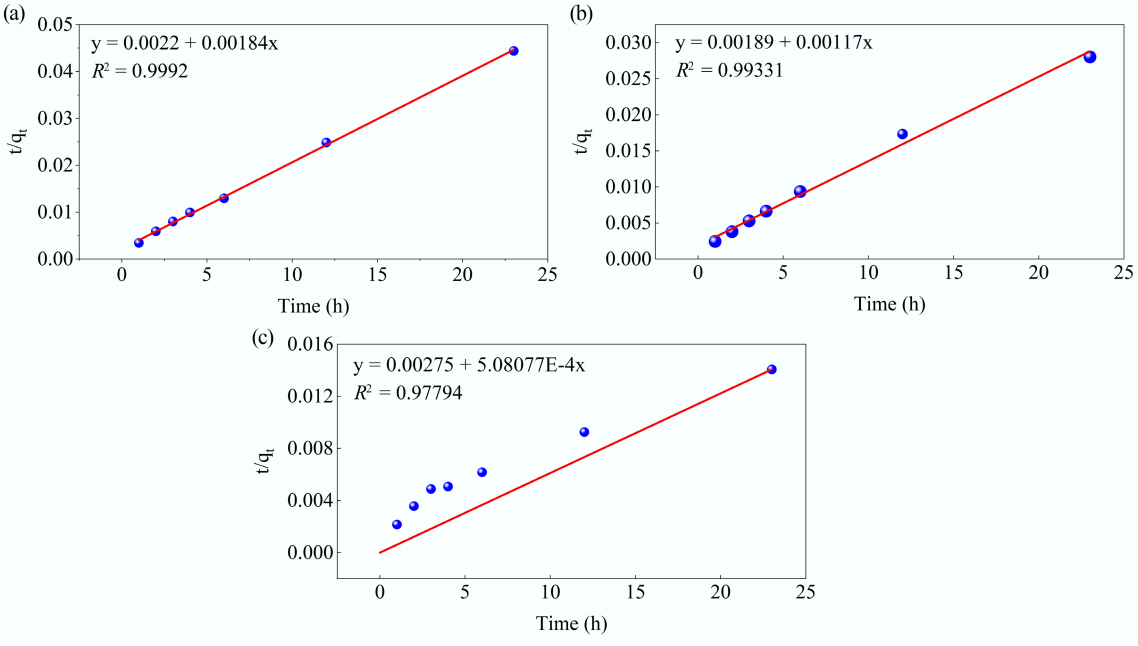

Fig. 12 Kinetic fits for MB adsorption on MAHC at (**a**) 24 °C, (**b**) 34 °C, and (**c**) 44 °C, using the pseudo-second-order model.

https://doi.org/10.48130/scm-0026-0014

Table 5 Kinetic model fitting parameters for the pseudo-first-order and pseudo-second-order models

T	Pseudo-first-order			Pseudo-second-order		
	q_e (mg/g)	k_1 (min^{-1})	R^2	q_e (mg/g)	k_2 (min^{-1})	R^2
24 °C	299.8643	0.20532	0.86046	543.4783	0.001539	0.9992
34 °C	463.8448	0.85966	0.73901	854.7009	0.000724	0.9931
44 °C	1437.47	0.12354	0.98077	1968.206	9.39E-05	0.9779

Table 6 Kinetic model fitting parameters for the intraparticle diffusion model

Temperature	Stage	Kp (mg/(g·min$^{1/2}$))	C (mg/g)	R^2
24 °C	First stage	289.7151	0	1
	Second stage	118.5603	169.5876	0.99787
	Third stage	23.48912	404.37198	0.99186
34 °C	First stage	379.8602	6.56063	0.9974
	Second stage	109.46267	376.3959	0.98987
	Third stage	77.83848	439.9813	0.97312
44 °C	First stage	340.61243	73.82852	0.98758

44 °C, the kinetics of three individual diffusion steps as observed at 24 and 34 °C cannot be distinguished because the temperature plays a role in diffusion by increasing the kinetic energy of the adsorbate molecules and lowering solution viscosity. This can help lower the resistance to mass transfer and make the adsorbate molecules move faster, which is evidenced by a higher value of K_p and a relatively lower value of C.

Proposed MB adsorption mechanisms

The adsorption of MB over MAHC can be achieved by both physical and chemical adsorption, as confirmed by the kinetic study. As illustrated by BET (see Fig. 1), and SEM analysis (see Fig. 2), MAHC showed a porous structure with a large specific surface area (1,266.1 m^2/g), which makes it easily accessible to MB and promotes physical adsorption onto the surface of the adsorbent. A similar finding was reported by Wang et al.[56]. To further prove this finding, BET analysis of the used MAHC was carried out, and the results are shown in Fig. 14. It can be seen that the specific surface area and total pore volume were reduced from 1,266.1 to 97.0 m^2/g and from 0.7394 to 0.1369 cm^3/g, respectively. Based on this observation, pore filling can be proven to be one of the adsorption mechanisms.

To further understand another possible mechanism of MB adsorption onto MAHC, the surface interaction between MB and MAHC before and after the adsorption experiment was investigated using XPS. Initially, based on the survey scan results (see Fig. 15), it can be clearly found that the peaks related to the XPS spectra of Fe 2p and Cu 2p3 were significantly changed in the used MAHC. The result suggests that Fe and Cu nanoparticles participated in the MB adsorption process, which could be due to the chemical interaction between the specific active sites provided by Fe and Cu nanoparticles and the functional groups of MB through surface complexation and the formation of chemical bonds. To further investigate, the Fe and Cu peaks were deconvoluted, and the results are given in Supplementary Fig. S3.

In addition, an N1s peak at 400.36 eV was observed in the used MAHC (Supplementary Fig. S4) but was absent in the fresh MAHC. This could be attributed to the N atoms of the adsorbed MB. The binding energy of 400.36 eV is higher than the binding energy of pure MB (i.e., 399.2 ± 0.2 eV), which could be related to the positively charged quaternary ammonium structure of methylene blue. This indicates that the N in MB was in a more electron-deficient environment because of the interaction with the Fe and Cu active sites and/or C. Because N in MB is positively charged, its electron density was pulled away by Fe/Cu and/or C, making it become electron-deficient and thus leading to an increase in XPS binding energy. This can be proven by the appearance of a deconvoluted C–N peak in the used MAHC at 285.66 eV, a peak that was absent in the fresh MAHC.

As depicted in Supplementary Fig. S5, the deconvolution of the C 1s spectra in fresh MAHC shows peaks corresponding to –C=C at 284.30 eV, –C–C and C–H at 284.80 eV, –C–OH and C–O–C at 286.30 eV, –C=O at 287.80 eV, and –O–C=O at 289.46 eV. For comparison, in the used MAHC, –C–C and C–H at 284.80 eV, –C–OH

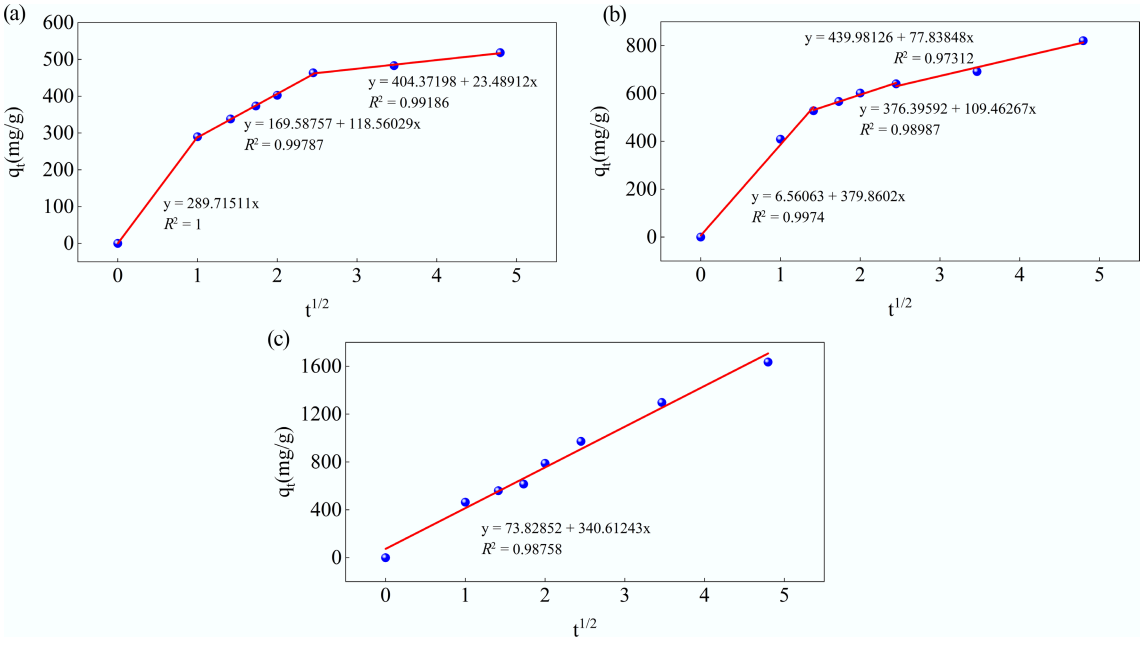

Fig. 13 Kinetic fits for MB adsorption on MAHC at (**a**) 24 °C, (**b**) 34 °C, and (**c**) 44 °C using the intraparticle diffusion model.

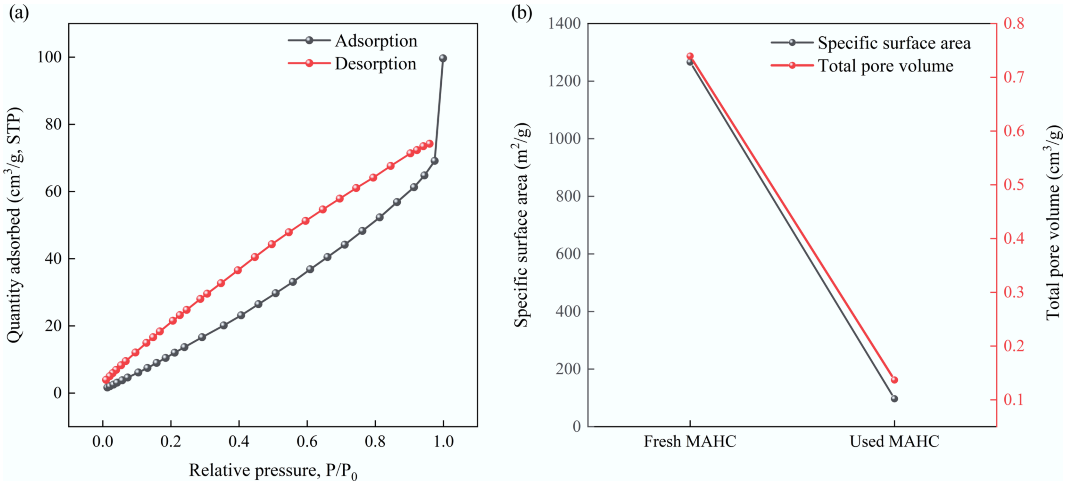

Fig. 14 (**a**) Adsorption/desorption isotherm of used MAHC, and (**b**) comparison of specific surface area and total pore volume between fresh MAHC and used MAHC.

and C–O–C at 286.30 eV, and –C=O at 287.80 eV were also observed. However, the –C=C peak was absent in the used MAHC. This could be attributed to the π-π interaction between the aromatic ring of MB and the C skeleton sheet of MAHC. As mentioned earlier, a new peak corresponding to C–N was found in the used MAHC. The –O–C=O peak shifted from 289.46 eV (fresh MAHC) to 289.39 eV (used MAHC). The reduced binding energy may indicate higher electron density of the O atom, as N is more electronegative and tends to accept electrons, while O donates electron pairs[56].

The deconvolution of O 1s spectra in fresh MAHC showed peaks at 529.95 eV (metal oxide), 531.26 eV (metal oxide, adventitious), and 532.41 eV (sulfate, adventitious), as displayed in Supplementary Fig. S6. On the other hand, in the used MAHC, two deconvoluted O 1s peaks were observed at 531.05 and 532.64 eV, respectively. Clearly, the deconvolution results of O 1s between fresh and used MAHC are different. The differences could be attributed to electronic transfer between N^+ in MB and metal oxides, or –O–C=O in MAHC[57].

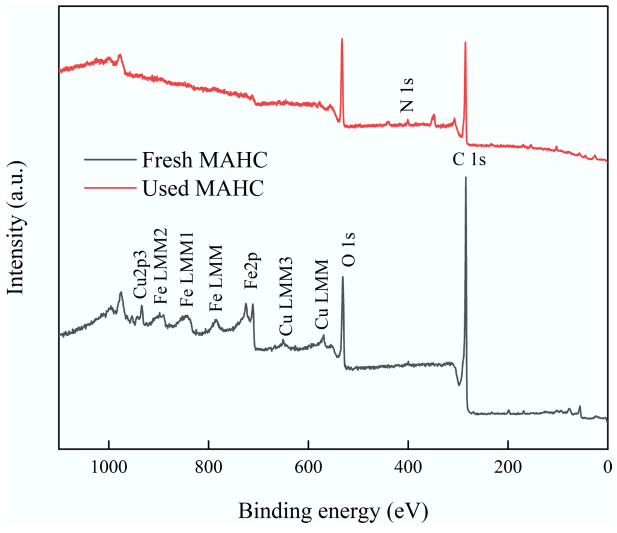

Fig. 15 XPS survey scan results of MAHC before and after MB adsorption.

Continuous adsorption experiment of MAHC for wastewater treatment

The continuous adsorption experiment of MAHC was conducted initially for the MB solution at room temperature for 180 min, followed by the test of real wastewater supplied by a local potato processing facility. The breakthrough curve, which represents the concentration of contaminants in the effluent of a column over time, indicates how the adsorbent changes as it becomes saturated. The breakthrough curve for the MB solution is given in Fig. 16. It can be seen that the MAHC reached a breakthrough point at 165 min, as shown in Fig. 17. For real wastewater, Fig. 18 indicates that the electrical conductivity and concentration of N, P, and K of effluent at 360 min (the last sampling time) are 2,652 μS/cm, 564 mg/kg, and 1,164 mg/kg, respectively, which are similar to the initial influent (as shown in Table 1).

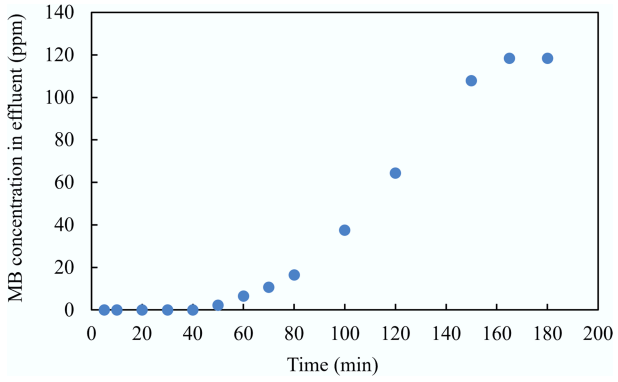

Fig. 16 Breakthrough curve of MAHC to treat the MB solution.

Fig. 17 MB adsorption experiment in a fixed bed column over 180 min.

https://doi.org/10.48130/scm-0026-0014

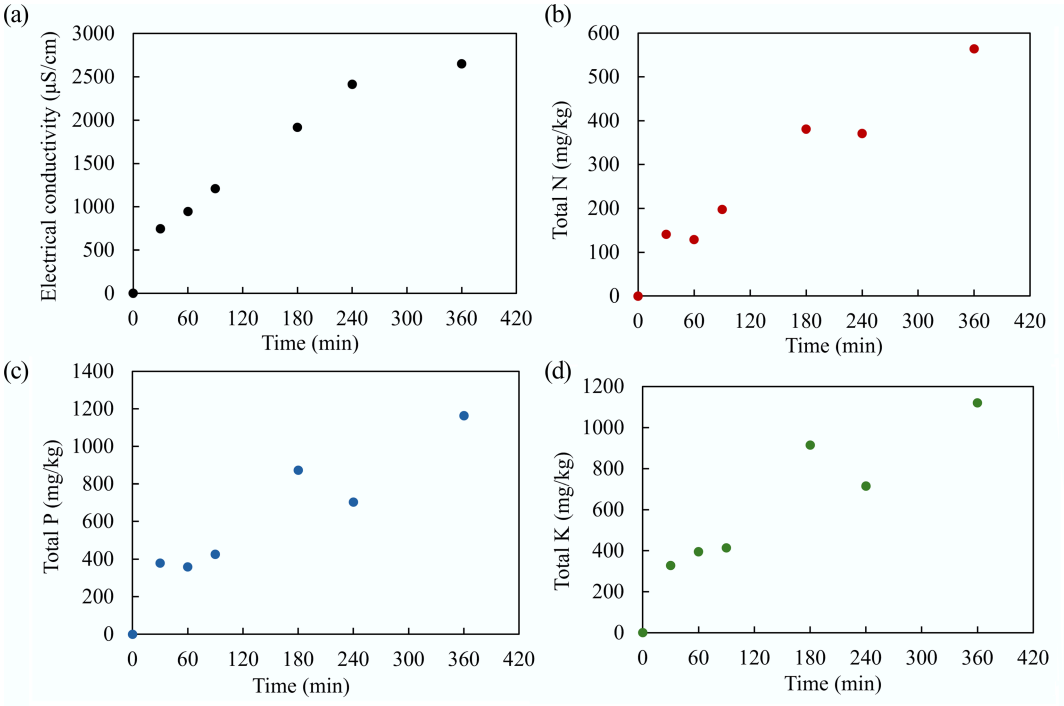

Fig. 18 (**a**) Electrical conductivity, and the concentration of (**b**) total N, (**c**) total P, and (**d**) total K in the effluent over 360 min.

Several limitations of this work have been identified: (1) the variability in feedstock characteristics could affect the properties of MAHC and consequently its performance in adsorbing MB from solution and cleaning up wastewater. This work is limited to the use of wood sawdust as the raw material, but it would be worthwhile to evaluate other types of feedstock, particularly third-generation biomass like microalgae and seaweed, in order to understand the influence of feedstock characteristics on adsorption performance; (2) although this work included adsorption experiments in both batch and continuous mode, future studies should carry out a comparative study to compare the adsorption performance of MAHC with that of commercial activated carbon; and (3) aside from a high adsorption capacity under optimized conditions, the high stability and recyclability are important properties for any type of adsorbent materials. This leads to another major limitation of the current work, i.e., the lack of study on the stability and recyclability of MAHC for adsorbing MB from solution and cleaning real wastewater, an issue which must be addressed in future work.

Conclusions

In this study, the bimetallic activated hydrochar was synthesized from sawdust to conduct adsorption using both batch and fixed-bed column experiments to remove MB and treat real wastewater. The main conclusions drawn from this study are given below.

• The highest adsorption capacity of MAHC of 1,635.28 mg/g was achieved at a pH of 10, an MB concentration of 50 ppm, an MAHC amount of 5 ppm, and a temperature of 44 °C.

• The Freundlich model fitted the experimental data better than the Langmuir and Temkin models, indicating that multilayer adsorption on a heterogeneous surface with a non-uniform distribution of adsorption heat is more dominant in MB adsorption using MAHC.

• The Pseudo-second-order model provided a better fit than the pseudo-first-order model, implying that the MB adsorption onto MAHC is a complex process.

• The intraparticle diffusion model suggests that adsorption occurred in three stages at 24 and 34 °C, but these stages were not observed at 44 °C, which suggests that higher temperatures lower resistance to mass transfer and allow adsorbate molecules to move faster.

• For the MB adsorption mechanism using MAHC, as evidenced by BET and XPS analysis, pore filling and surface interaction, such as the interaction between Fe and Cu active sites and MB and π-π interaction, were found to be the dominant mechanisms for MB adsorption onto MAHC. However, electrostatic attraction was not significant, since the influence of pH on MB adsorption capacity was minor.

• In the fixed-bed column experiments, the breakthrough point was achieved at 165 and 360 min for the MB solution and real wastewater, respectively.

Supplementary information

It accompanies this paper at: https://doi.org/10.48130/scm-0026-0014.

Author contributions

The authors confirm their contributions to the paper as follows: Milad Jalilian: study conception and design, data collection, analysis and interpretation of results, draft manuscript preparation; Bisma Nawazish: study conception and design, data collection; Regiane Taborda: study conception and design, data collection; Quan Sophia He: manuscript revision; Yulin Hu: manuscript revision. All authors reviewed the results and approved the final version of the manuscript.

Data availability

The datasets generated during and/or analyzed during the current study are available from the corresponding author on reasonable request.

Acknowledgement

The authors are grateful for the Natural Science and Engineering Research Council (NSERC), Canada, and Mitacs Global link program.

Funding

This work was financially supported by Discovery Grants (Grant numbers: RGPIN-2022-03203 and RGPIN-2020-05695) and the Mitacs Global link program (Project ID: 45224 and Project ID: 45223).

Declarations

Competing interests

The authors declare that they have no conflict of interest.

Author details

[1]Faculty of Sustainable Design Engineering, University of Prince Edward Island, Charlottetown, PE, C1A 4P3, Canada; [2]Department of Engineering, Dalhousie University, Truro, NS, B2N 5E3, Canada

References

[1] Fathi A, Asgari E, Danafar H, Salehabadi H, Fazli MM. 2024. A comprehensive study on methylene blue removal *via* polymer and protein nanoparticle adsorbents. *Scientific Reports* 14:29434

[2] Wang Y, Zheng J, Zhou T, Zhang Q, Feng M, et al. 2025. Confinement-modulated singlet-oxygen nanoreactors for water decontamination. *Environmental Science & Technology* 59(12):6341−6351

[3] Dang C, Wu Z, Fu J. 2023. Environmental issues caused by high-dose disinfection need urgent attention. *Environment & Health* 1(1):3−5

[4] Rashid R, Shafiq I, Akhter P, Iqbal MJ, Hussain M. 2021. A state-of-the-art review on wastewater treatment techniques: the effectiveness of adsorption method. *Environmental Science and Pollution Research* 28(8):9050−9066

[5] Gęca M, Wiśniewska M, Nowicki P. 2022. Biochars and activated carbons as adsorbents of inorganic and organic compounds from multicomponent systems–a review. *Advances in Colloid and Interface Science* 305:102687

[6] Wang B, Lan J, Bo C, Gong B, Ou J. 2023. Adsorption of heavy metal onto biomass-derived activated carbon: review. *RSC Advances* 13(7):4275−4302

[7] Bednárek J, Matějová L, Koutník I, Vráblová M, Cruz GJF, et al. 2024. Revelation of high-adsorption-performance activated carbon for removal of fluoroquinolone antibiotics from water. *Biomass Conversion and Biorefinery* 14(2):2585−2599

[8] Zieliński B, Miądlicki P, Przepiórski J. 2022. Development of activated carbon for removal of pesticides from water: case study. *Scientific Reports* 12:20869

[9] Agarwal AM, Kadu MS, Pandhurnekar CP, Muthreja IL. 2014. Langmuir Freudlich and BET adsorption isoterm studies for zink icon onto coal fly ash. *International Journal of Innovation Engineering & Management* 3:64−71

[10] Abdullah MO, Tan IAW, Lim LS. 2011. Automobile adsorption air-conditioning system using oil palm biomass-based activated carbon: a review. *Renewable and Sustainable Energy Reviews* 15(4):2061−2072

[11] Yi H, Nakabayashi K, Yoon SH, Miyawaki J. 2021. Pressurized physical activation: a simple production method for activated carbon with a highly developed pore structure. *Carbon* 183:735−742

[12] Yu S, He J, Zhang Z, Sun Z, Xie M, et al. 2024. Towards negative emissions: hydrothermal carbonization of biomass for sustainable carbon materials. *Advanced Materials* 36(18):e2307412

[13] Khoshbouy R, Takahashi F, Yoshikawa K. 2019. Preparation of high surface area sludge-based activated hydrochar *via* hydrothermal carbonization and application in the removal of basic dye. *Environmental Research* 175:457−467

[14] Sathe SM, Chakraborty I, Dubey BK, Ghangrekar MM. 2024. Wastewater sludge-derived hydrochar: effect of operating conditions, activation, and potential use as adsorbent. *Process Safety and Environmental Protection* 184:1400−1410

[15] Meng H, Chen Z, Wei W, Xu J, Duan H, et al. 2025. Magnetic hydrochar for sustainable wastewater management. *npj Materials Sustainability* 3:7

[16] Bharti V, Vikrant K, Goswami M, Tiwari H, Sonwani RK, et al. 2019. Biodegradation of methylene blue dye in a batch and continuous mode using biochar as packing media. *Environmental Research* 171:356−364

[17] Cheng J, Zhan C, Wu J, Cui Z, Si J, et al. 2020. Highly efficient removal of methylene blue dye from an aqueous solution using cellulose acetate nanofibrous membranes modified by polydopamine. *ACS Omega* 5(10):5389−5400

[18] Ahmad NN, Ahmad AA, Khasri A. 2023. Effective removal of methylene blue from aqueous solution by adsorption onto gasification char: isotherm, kinetic and thermodynamics studies. *Desalination and Water Treatment* 285:264−273

[19] Halim OMA, Mustapha NH, Mohd Fudzi SN, Azhar R, Zanal NIN, et al. 2025. A review on modified ZnO for the effective degradation of methylene blue and rhodamine B. *Results in Surfaces and Interfaces* 18:100408

[20] Jalilian M, He QS, Hu Y. 2026. Synthesis of bimetallic biocomposite materials prepared from activated hydrochar/biochar for methylene blue removal *via* Fenton oxidation coupled with adsorption. *Chemical Engineering Science* 320:122514

[21] Pallarés J, González-Cencerrado A, Arauzo I. 2018. Production and characterization of activated carbon from barley straw by physical activation with carbon dioxide and steam. *Biomass and Bioenergy* 115:64−73

[22] Liu S, Zheng LN, Dong SW, Sun YZ, Xue N, et al. 2025. Selective adsorption and efficient separation of methylene blue dye in a water-stable nickel-based metal–organic framework. *Separation and Purification Technology* 376:134057

[23] Santoso E, Ediati R, Kusumawati Y, Bahruji H, Sulistiono DO, et al. 2020. Review on recent advances of carbon based adsorbent for methylene blue removal from waste water. *Materials Today Chemistry* 16:100233

[24] Ahmed MJ, Dhedan SK. 2012. Equilibrium isotherms and kinetics modeling of methylene blue adsorption on agricultural wastes-based activated carbons. *Fluid Phase Equilibria* 317:9−14

[25] Serafin J, Dziejarski B. 2023. Application of isotherms models and error functions in activated carbon CO_2 sorption processes. *Microporous and Mesoporous Materials* 354:112513

[26] Zhang X, Xiong S, Sathiyaseelan A, Zhang L, Lu Y, et al. 2024. Recent advances in photocatalytic nanomaterials for environmental remediation: strategies, mechanisms, and future directions. *Chemosphere* 364:143142

[27] Wang T, Jiang M, Yu X, Niu N, Chen L. 2022. Application of lignin adsorbent in wastewater Treatment: a review. *Separation and Purification Technology* 302:122116

[28] Robati D. 2013. Pseudo-second-order kinetic equations for modeling adsorption systems for removal of lead ions using multi-walled carbon nanotube. *Journal of Nanostructure in Chemistry* 3(1):55

[29] ASTM International. 2014. *Standard test method for determination of iodine number of activated carbon*. Annual Book of ASTM Standard Test Method

[30] Tran TH, Le AH, Pham TH, Nguyen DT, Chang SW, et al. 2020. Adsorption isotherms and kinetic modeling of methylene blue dye onto a carbonaceous hydrochar adsorbent derived from coffee husk waste. *Science of The Total Environment* 725:138325

[31] Ebadollahzadeh H, Zabihi M. 2020. Competitive adsorption of methylene blue and Pb (II) ions on the nano-magnetic activated carbon and alumina. *Materials Chemistry and Physics* 248:122893

[32] Han Q, Wang J, Goodman BA, Xie J, Liu Z. 2020. High adsorption of methylene blue by activated carbon prepared from phosphoric acid treated *Eucalyptus* residue. *Powder Technology* 366:239−248

[33] El Jery A, Alawamleh HSK, Sami MH, Abbas HA, Sammen SS, et al. 2024. Isotherms, kinetics and thermodynamic mechanism of methylene blue dye adsorption on synthesized activated carbon. *Scientific Reports* 14:970
[34] Shu J, Cheng S, Xia H, Zhang L, Peng J, et al. 2017. Copper loaded on activated carbon as an efficient adsorbent for removal of methylene blue. *RSC Advances* 7(24):14395−14405
[35] Oliveira LCA, Rios RVRA, Fabris JD, Garg V, Sapag K, et al. 2002. Activated carbon/iron oxide magnetic composites for the adsorption of contaminants in water. *Carbon* 40(12):2177−2183
[36] Mahapatra K, Ramteke DS, Paliwal LJ. 2012. Production of activated carbon from sludge of food processing industry under controlled pyrolysis and its application for methylene blue removal. *Journal of Analytical and Applied Pyrolysis* 95:79−86
[37] Saka C. 2012. BET, TG–DTG, FT-IR, SEM, iodine number analysis and preparation of activated carbon from acorn shell by chemical activation with $ZnCl_2$. *Journal of Analytical and Applied Pyrolysis* 95:21−24
[38] Cheng S, Zhang L, Ma A, Xia H, Peng J, et al. 2018. Comparison of activated carbon and iron/cerium modified activated carbon to remove methylene blue from wastewater. *Journal of Environmental Sciences* 65:92−102
[39] Kriegseis S, Vogl AY, Aretz L, Tonnesen T, Telle R. 2020. *Zeta* potential and long-term stability correlation of carbon-based suspensions for material jetting. *Open Ceramics* 4:100037
[40] Altıntıg E, Altundag H, Tuzen M, Sarı A. 2017. Effective removal of methylene blue from aqueous solutions using magnetic loaded activated carbon as novel adsorbent. *Chemical Engineering Research and Design* 122:151−163
[41] Karaer H, Kaya İ. 2016. Synthesis, characterization of magnetic chitosan/active charcoal composite and using at the adsorption of methylene blue and reactive blue4. *Microporous and Mesoporous Materials* 232:26−38
[42] Xu JC, Xin PH, Han YB, Wang PF, Jin HX, et al. 2014. Magnetic response and adsorptive properties for methylene blue of $CoFe_2O_4$/Co x Fe y/activated carbon magnetic composites. *Journal of Alloys and Compounds* 617:622−626
[43] Lee H, Fiore S, Berruti F. 2024. Adsorption of methyl orange and methylene blue on activated biocarbon derived from birchwood pellets. *Biomass and Bioenergy* 191:107446
[44] Yao Y, Xu F, Chen M, Xu Z, Zhu Z. 2010. Adsorption behavior of methylene blue on carbon nanotubes. *Bioresource Technology* 101(9):3040−3046
[45] Ghaedi M, Nasab AG, Khodadoust S, Rajabi M, Azizian S. 2014. Application of activated carbon as adsorbents for efficient removal of methylene blue: kinetics and equilibrium study. *Journal of Industrial and Engineering Chemistry* 20(4):2317−2324
[46] Hien Tran T, Le AH, Pham TH, Duong LD, Nguyen XC, et al. 2022. A sustainable, low-cost carbonaceous hydrochar adsorbent for methylene blue adsorption derived from corncobs. *Environmental Research* 212:113178
[47] Qian WC, Luo XP, Wang X, Guo M, Li B. 2018. Removal of methylene blue from aqueous solution by modified bamboo hydrochar. *Ecotoxicology and Environmental Safety* 157:300−306
[48] Islam MA, Ahmed MJ, Khanday WA, Asif M, Hameed BH. 2017. Mesoporous activated coconut shell-derived hydrochar prepared *via* hydrothermal carbonization-NaOH activation for methylene blue adsorption. *Journal of Environmental Management* 203:237−244
[49] Do TH, Nguyen VT, Dung NQ, Chu MN, Van Kiet D, et al. 2021. Study on methylene blue adsorption of activated carbon made from *Moringa oleifera* leaf. *Materials Today: Proceedings* 38:3405−3413
[50] Gupta SA, Vishesh Y, Sarvshrestha N, Bhardwaj AS, Kumar PA, et al. 2022. Adsorption isotherm studies of Methylene blue using activated carbon of waste fruit peel as an adsorbent. *Materials Today: Proceedings* 57:1500−1508
[51] Al-Musawi EB, Al-Qaim FF. 2025. Elimination of methylene blue dye from the aqueous solution using waste fig fruit as an activated carbon: a case study of nonlinear adsorption isotherm models and kinetic models. *Reaction Kinetics, Mechanisms and Catalysis* 138(2):967−989
[52] Buhani, Dewi JS, Fajriyah NS, Rilyanti M, Suharso, et al. 2023. Modification of non-activated carbon from rubber fruit shells with 3-(aminopropyl)-triethoxysilane and its adsorption study on coomassie brilliant blue and methylene blue in solution. *Water, Air, & Soil Pollution* 234(9):578
[53] Lyu H, Gao B, He F, Zimmerman AR, Ding C, et al. 2018. Experimental and modeling investigations of ball-milled biochar for the removal of aqueous methylene blue. *Chemical Engineering Journal* 335:110−119
[54] de Souza CC, de Souza LZM, Yılmaz M, de Oliveira MA, da Silva Bezerra AC, et al. 2022. Activated carbon of *Coriandrum* sativum for adsorption of methylene blue: equilibrium and kinetic modeling. *Cleaner Materials* 3:100052
[55] Bouchelkia N, Tahraoui H, Amrane A, Belkacemi H, Bollinger JC, et al. 2023. Jujube stones based highly efficient activated carbon for methylene blue adsorption: kinetics and isotherms modeling, thermodynamics and mechanism study, optimization *via* response surface methodology and machine learning approaches. *Process Safety and Environmental Protection* 170:513−535
[56] Wang Q, Fagbohun EO, Zhu H, Hussain A, Wang F, et al. 2023. One-step synthesis of magnetic asphalt-based activated carbon with high specific surface area and adsorption performance for methylene blue. *Separation and Purification Technology* 321:124205
[57] Qin N, Tian C, Carter L, Tao D, Zhou Y, et al. 2024. Economical magnetic activated carbon for methylene blue removal from water. *Next Sustainability* 4:100057